Article

Laterally extended states of interlayer excitons in reconstructed MoSe$_2$/WSe$_2$ heterostructures

Check for updates

Johannes Figueiredo[1,2], Marten Richter[3] ✉, Mirco Troue[1,2], Jonas Kiemle[1,2], Hendrik Lambers[4],
Torsten Stiehm[4], Takashi Taniguchi[5], Kenji Watanabe[6], Ursula Wurstbauer[4], Andreas Knorr[3] ✉ &
Alexander W. Holleitner[1,2] ✉

Heterostructures made from 2D transition-metal dichalcogenides are known as ideal platforms to explore excitonic phenomena ranging from correlated moiré excitons to degenerate interlayer exciton ensembles. So far, it is assumed that the atomic reconstruction appearing in some of the heterostructures gives rise to a dominating localization of the exciton states. We demonstrate that the center-of-mass wavefunction of the excitonic states in reconstructed MoSe$_2$/WSe$_2$ heterostructures can extend well beyond the moiré periodicity of the investigated heterostructures. The results are based on real-space calculations yielding a lateral potential map for interlayer excitons within the strain-relaxed heterostructures with weak random disorder, as expected for realistic samples, and the corresponding real-space center-of-mass excitonic wavefunctions. We combine the theoretical results with cryogenic photoluminescence experiments, which support the computed level structure and relaxation characteristics of the interlayer excitons.

Monolayers of group-VI transition-metal dichalcogenides (TMDs) have risen to prominence in solid-state research for over a decade due to their unique light-matter interactions[1–3]. The optical response of TMDs and their van der Waals heterostructures is dominated by Coulomb-bound electron-hole pairs, known as excitons, that can be tuned by dielectric engineering, doping and heterostructuring and are subjected to rich interaction as well as spin- and multivalley physics[4–9]. A prominent example are interlayer excitons (IXs), which particularly form across the interface of a type-II band alignment such as in MoSe$_2$/WSe$_2$ heterostructures[8–13]. The corresponding spatial separation of the electron and hole in adjacent layers gives rise to an increased out-of-plane electric dipole and a reduction of their wavefunction's spatial overlap. The latter significantly enhances the radiative lifetimes of the IXs to the order of tens to hundreds of nanoseconds[8,9]. Moreover, lateral moiré superlattices emerge in lattice-mismatched and/or twisted TMD hetero-bilayers and -trilayers[14–17]. At small twist angles and/or small lattice mismatches, reconstructions can lead to the formation of lateral domains with a rather constant atomic registry and a corresponding potential landscape for electrons and holes, which typically results in

strongly localized excitons[16–20]. While the long lifetimes and the out-of-plane electric dipole position IXs as promising candidates for studying many-body phenomena across a large range of density regimes[21], many findings are assumed to be limited by localization effects[7,19,22–26].

The present work aims to explain the impact of reconstruction on the excitonic wavefunction in real space. A particular question is whether spatially extended IX states can evolve in reconstructed heterostructures at certain twist angles. Generally, the amplitude of the periodic potential landscape changes as a function of the twist angle. Recent studies suggest much lower energy amplitudes in the potential landscape for IXs in H-type MoSe$_2$/WSe$_2$ heterostructures (twist angle close to 60°) than in R-type ones (twist angle close to 0°)[27]. We combine theoretical calculations of excitonic states in reconstructed MoSe$_2$/WSe$_2$ heterostructures close to 60° with experimental photoluminescence measurements on correspondingly designed samples. The calculations yield a two-dimensional potential landscape for the IXs within the relaxed heterostructures and a real-space representation of the IX center-of-mass wavefunctions of electrons and holes, as well as theoretical linear absorption and photoluminescence

¹Walter Schottky Institute and Physics Department, Technical University of Munich, Am Coulombwall 4a, Garching, 85748, Germany. ²Munich Center for Quantum Science and Technology (MCQST), Schellingstr. 4, Munich, 80799, Germany. ³Institut für Physik und Astronomie, Nichtlineare Optik und Quantenelektronik, Technische Universität Berlin, Hardenbergstr. 36, EW 7-1, Berlin, 10623, Germany. ⁴Institute of Physics and Center for Soft Nanoscience (SoN), University of Münster, Wilhelm-Klemm-Str. 10, Münster, 48149, Germany. ⁵International Center for Materials Nanoarchitectonics, National Institute for Materials Science, Tsukuba, 305-0044, Japan. ⁶Research Center for Functional Materials, National Institute for Materials Science, Tsukuba, 305-0044, Japan.
✉e-mail: marten.richter@tu-berlin.de; andreas.knorr@tu-berlin.de; holleitner@wsi.tum.de

spectra of the IXs in the energy and time domains. The theory is formulated in real space, covering several moiré unit cells to simulate a spatially inhomogeneous exciton distribution. Most importantly, the lateral extension of the wavefunction of the first IX eigenstates suggests delocalized excitons over more than a hundred nanometers, particularly for twist angles larger than 1.3° with respect to 60°. Therefore, the delocalized IXs extend well beyond the moiré periodicity and are impacted by potential fluctuations within the two-dimensional plane. Moreover, the energetically lowest states located in different moiré unit cells form a single luminescence peak, which particularly dominates the calculated photoluminescence in the quasi-equilibrium regime. At smaller twist angles with respect to 60°, the calculated depth of the exciton potential increases, leading to a distribution of clearly localized exciton states, as it is consistent with earlier work[28,29]. Moreover, depending on the twist angle, the type of localized states covers quantum dot-like states to networks of quantum wire-like states, again in agreement with literature[7]. A relatively small twist angle variation can utterly change the nature of the exciton states, forming the described resonances in photoluminescence for small twist angles close to 60°. The calculations are consistent with the presented photoluminescence experiments performed on several samples. We present low-power and time-resolved photoluminescence spectra of IXs at cryogenic temperatures, suggesting that the investigated exciton ensembles are in a dilute regime. The temporal evolution of the photoluminescence after excitation shows higher IX luminescence peaks with a distinct spectrum, which is consistent with the theoretical results. The overall observed Lorentzian-type lineshape supports the interpretation of a spatially extended IX ground state within the plane of the heterostructure for twist angles close to 60°.

Results

Experimental photoluminescence

We experimentally investigate three different samples with similar photoluminescence properties, all of which consist of an hBN-encapsulated $MoSe_2/WSe_2$ H-type heterostructure at a twist angle close to 60°, as determined independently by magneto-photoluminescence measurements (cf. Figs. S1 and S2). For the rest of the manuscript, all twist angles mentioned are given as a relative deviation from the ideal 60° of a typical H-type heterostructure. Figure 1a depicts a scheme of the investigated heterostructure highlighting an IX, where the hole and the electron reside in the different TMD monolayers. We utilize a pump laser at an energy of $E_{laser} = 1.94$ eV to excite the charge carriers in both monolayers, thus forming IXs. Figure 1b shows the resulting photoluminescence spectra for excitation powers from 722 nW down to 778 fW, where the luminescence signal is close to the overall noise floor. The single luminescence peak at $E_{IX} = 1.398$ eV is interpreted as the recombination of IXs, and it keeps a sharp Lorentzian-type lineshape with a FWHM ≈ 4 meV throughout the investigated range of excitation powers. Figure S2 shows the power series of photoluminescence spectra on the two other samples. For all three samples, the photon count of the low-power spectra suggests a small IX density in the dilute, single-exciton regime. Moreover, the lack of a blueshift of the emission energy with increasing pump power supports this interpretation of having IXs within the dilute regime, where mutual interactions between excitons can be neglected. Given the long photoluminescence lifetime of several tens of ns, we interpret the underlying IX states as the excitonic ground states at the chosen positions of the three samples, respectively[30,31]. We further observe that the single luminescence peaks with a sharp Lorentzian-type lineshape as in Fig. 1b exhibit a spatial profile that exceeds the point-spread function of the utilized optical system by hundreds of nanometers even in the dilute, single-exciton regime (cf. Fig. S3).

Calculation of exciton states in strained heterostructures

In the next step, we complement the experimental results with theoretical calculations of H-type heterostacks of MoSe₂ and WSe₂ monolayers. The underlying theoretical model including the used parameters is described in ref. 32, which contains calculations of linear spectra for R-type
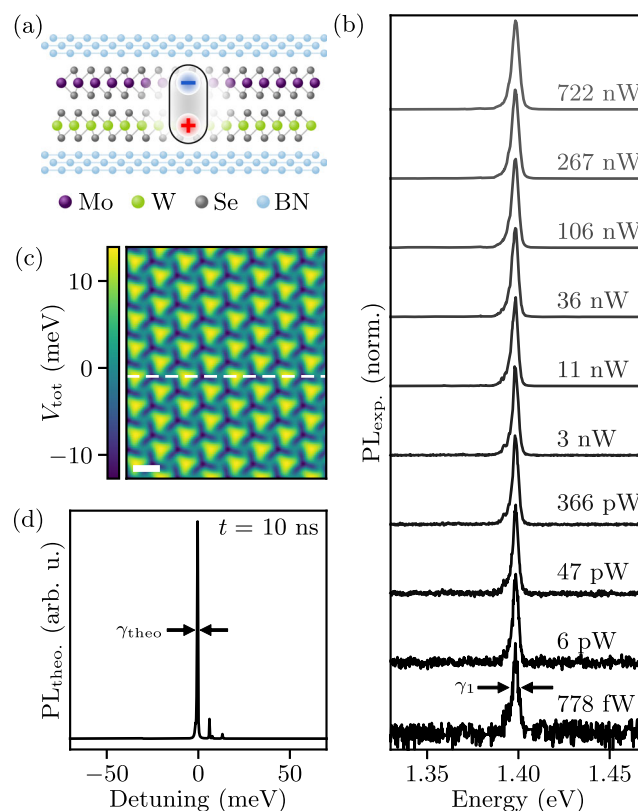

Fig. 1 | Interlayer excitons in H-type MoSe₂/WSe₂ heterostructures. a Schematic side-view of a MoSe₂/WSe₂ heterostructure encapsulated in hBN, featuring an interlayer exciton (IX). **b** Power series of experimental photoluminescence spectra at a bath temperature of $T_{bath}^{exp} = 1.65$ K. The IXs emit light at $E_{IX} = 1.398$ eV with a singular Lorentzian-type shape with a full-width-at-half-maximum (FWHM) γ_1. The lineshape is retained down to the lowest investigated excitation powers. **c** Simulated total potential V_{tot} landscape within the x–y plane of a strain relaxed, reconstructed bilayer at a twist angle of 1.3° wrt. 60°. The dashed line highlights a certain crystal direction, as discussed in the text. Scale bar marks 10 nm. **d** Averaged theoretical photoluminescence spectrum with an apparent FWHM of γ_{theo} at a time delay of 10 ns after the excitation and a theoretical bath temperature of $T_{bath}^{theo} = 1.65$ K. Note that a zero detuning describes the lowest 1s IX energy without any influence from strain potentials.

heterostructures. The model starts with a continuum mechanics theory to describe the lattice relaxation leading to reconstruction (based on refs. 20,32,33). The calculated displacement and strain fields form a potential for electrons and holes, which allows the calculation of interlayer states. Instead of the frequently used quasi-momentum space, the exciton states are calculated in real space to capture the effects of imperfections and disorder that disrupt translational symmetry within the plane of the heterostructures[32,34,35]. The interlayer states are used as the basis for a quantum dynamic model to describe the IXs, including exciton-phonon scattering. The quantum dynamic calculation incorporates rates using a Born-Markov approximation after polaron transformation to account for multi-phonon processes[32]. The calculation of optical spectra uses parameters from refs. 33,36–43. The utilized approach enables us to study the structure of both localized and spatially extended exciton states with respect to the center-of-mass motion of electrons and holes.

The calculation starts with the displacement field of the MoSe₂ and WSe₂ monolayers that form the top and bottom layers of the reconstructed lattice. The corresponding displacement field $u_{b/t}(r)$ of the bottom and top layers is obtained by minimizing the intra- and interlayer lattice energy[20,32,33], usually for an 8 x 4 supercell of the moiré structure[32]. We do not aim for perfect minimization, but leave some residual error to simulate the disorder present in the experimental samples. In turn, disorder does not come from

impurities or other sources in our model, but from slight imperfections of the reconstruction.

The relative interlayer displacement leads to a potential $V_{e/h}^{inter}(\mathbf{r})$ for electrons and holes[37]. We modified the formula from[37,38] such that $V_{e/h}^{inter}(\mathbf{r}_{e/h}) = V_{exc} \sum_{n=1}^{3} \cos(\varphi_n(\mathbf{r}_{e/h}) + \varphi_{exc,s})$, and that $\varphi_n(\mathbf{r})$ is also modified by the displacement field $u^{(t/b)}(\mathbf{r})$ of the top and bottom layer (please, see ref. 32 for the definitions and values of $V_{exc}\varphi_n(\mathbf{r}_{e/h})$ and $\varphi_{exc,s}$). Additionally, the intralayer strain created by lattice reconstruction leads to another contribution to the potential $V_{e/h}^{intra}(\mathbf{r})^{36}$ acting on electrons and holes, it has the form $V_{e/h}^{intra}(\mathbf{r}_{e/h}) = \Delta E_{gap}^{e/h} \left(\frac{\partial u_x}{\partial x} + \frac{\partial u_y}{\partial y} \right)$, where changes in displacement field $\mathbf{u}$ describe stress leading to a band gap change (cf.[32,36] for details). The formulas from refs. 36,37 were modified in ref. 32 to include displacement due to reconstruction. The modification shifts the current position in the interlayer potential by the strain fields. More details of the modification can be found in ref. 32. The total potential $V_{tot}(\mathbf{r}) = V_{intra}(\mathbf{r}) + \frac{1}{2}V_{inter}(\mathbf{r})$ is just the sum of the interlayer and intralayer contribution (the interlayer contribution is a band gap shift[38], which we distribute evenly to electrons and holes as an initial assumption[32]). Thus, $V_{tot}(\mathbf{r})$ describes the full strain potential.

For an exemplary twist angle deviation of 1.3°, the calculated potential landscape V_{tot} for IXs exhibits a periodic pattern [Fig. 1c]. The potential landscape matches experimental findings of a kagome-like lattice rearrangement dominated by hexagonal areas[16,17]. Moreover, the calculations predict the potential to feature shallow minima when compared to R-type heterostructures of the same materials, e.g. of around − 12 meV for 1.3°. Our theory also provides photoluminescence spectra (see below for the specific calculation of the spectra), which again consider the exciton–phonon interactions in the calculation. Exemplarily, Fig. 1d shows the calculated photoluminescence (PL$_{theo}$) for the already discussed 1.3° case at a time delay of 10 ns after initial injection of interlayer excitons and a theoretical temperature of $T_{bath}^{theo} = 1.65$ K. The time delay is long enough for the simulation to mimic a quasi-equilibrium near steady-state photoluminescence before a complete radiative recombination.

Generally, the exciton wavefunctions in real space must be calculated as a function of the spatial coordinates to understand the lateral characteristics of the excitonic states within the reconstructed heterostructures, including disorder. We start with a factorization of the exciton wavefunction $\Psi(\mathbf{r}_e, \mathbf{r}_h) = \psi(\mathbf{R})\phi(\mathbf{r})$ into the relative $\phi(\mathbf{r})$ and the center-of-mass (COM) $\psi(\mathbf{R})$ part. We obtain the 1s relative wavefunction $\phi_{1s}(\mathbf{r})$ after solving the Schrödinger equation $E\phi(\mathbf{r}) = \left[-\frac{\hbar^2}{2m_r}\Delta_r + V_{eh}(\mathbf{r}) \right]\phi(\mathbf{r})$ using finite differences with reduced mass m_r and a Rytova-Keldysh potential $V_{eh}(\mathbf{r})$ (cf.[32] for the used form and parameters). We include only one species of interlayer exciton and disregard its spin state. We calculate the potential $V_{COM}(\mathbf{R})$ acting on the COM wavefunction by convoluting the electron and hole potentials $V_e(\mathbf{r}) = V_h(\mathbf{r}) = V_{tot}(\mathbf{r})$ with $\phi_{1s}(\mathbf{r})$ (cf.[32,44]): $V_{COM}(\mathbf{R}) = \int d^2r |\phi_{1s}(\mathbf{r})|^2 \left[V_e\left(\mathbf{R} - \frac{m_h}{M}\mathbf{r}\right) + V_h\left(\mathbf{R} + \frac{m_e}{M}\mathbf{r}\right) \right]$ with total mass M and electron and hole masses m_e and m_h. We numerically compute the lowest 2500 eigenstates and eigenstates of the COM Schrödinger equation $\left[-\frac{\hbar^2}{2M}\Delta_R + V_{COM}(\mathbf{R}) \right]\psi(\mathbf{R}) = E\psi(\mathbf{R})$ for the COM wavefunction using finite differences as the basis for the COM exciton states. If the 2500 eigenstates do not cover the spectroscopically relevant states, we choose a smaller supercell (4 x 2 instead of 8 x 4). For the 1.3° example, Fig. 2a shows both the interlayer potential and the absolute value of the wavefunction of the first IX eigenstate along the white, dashed line of the reconstructed bilayer shown in Fig. 1c. Figure 2b–d gives the absolute values of the wavefunctions Ψ for the first three COM IX eigenstates as a function of the spatial coordinates x and y. Each wavefunction varies in space because of the impact of the small spatial imperfections of V_{tot} within the plane of the heterostructure [cf. arrow in Fig. 2a and details in Fig. S4]. For comparison, the red dashed line in Fig. 2b highlights the direction that resembles the x-axis of Fig. 2a.

In real experimental samples, there are often small twist angle deviations across the lateral extension of the sample. Therefore, we compare our
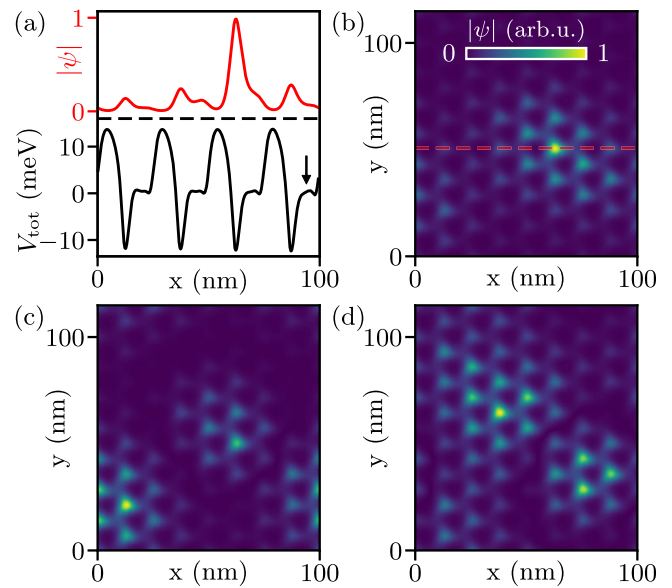

Fig. 2 | Real space representation of the center-of-mass wavefunction of the first excitonic states. a Top curve: absolute value of the center-of-mass (COM) wavefunction Ψ for the first COM IX eigenstate along the crystallographic direction of a reconstructed bilayer at 1.3° twist angle as shown in Fig. 1c. Bottom curve: Corresponding total IX potential along the same direction. The arrow indicates one of many small variations of V_{tot} caused by the introduced imperfections within the simulated sample. **b–d** Absolute value of the COM wavefunction of the first three IX eigenstates in real space. The dashed red line in (**b**) corresponds to the x-axis in (**a**).

results at 1.3° to those with a relative twist angle of 1.1° and 0.9° (cf. Fig. S5), which may manifest in other parts of a sufficiently large sample. Figure 3a–c depicts the absolute value of the real space COM wavefunction Ψ for each of the twist angles 1.3°, 1.1°, and 0.9°. Our results suggest that the qualitative nature of the lowest energy state changes from the 1.3° configuration towards slightly smaller twist angles. Particularly for 0.9°, the wavefunction seems to be localized within one moiré unit cell. To quantitatively capture this observation, Fig. 3d–f depicts the lateral size (calculated as $\sqrt{\langle(\mathbf{R} - \langle\mathbf{R}\rangle)^2\rangle}$) of the COM wavefunction for the 2500 lowest IX eigenstates for each of the three twist angles, as it is plotted as a function of the exciton energy excluding polaron shifts. Note that the maximal possible size in Fig. 3d–f is limited to the computational domain, so reaching the maximum effectively means a full delocalization of the corresponding state.

The calculated wavefunction extensions and an inspection of the COM wavefunction in real space show that the lowest energy eigenstate at 1.3° is already delocalized [Fig. 3a and red dot in Fig. 3d] and is thus not confined to one moiré unit cell (dashed line with expected moiré periodicity $a_m^{1.3°} = 14.3$ nm)[45]. This means that for 1.3° the influence of the moiré potential is so small that delocalized states are close to the case without a moiré potential. Such delocalization is not the case for smaller twist angles, as exemplarily shown in Fig. 3e, f, where the first states are small and rather localized inside a moiré unit cell at the respective angles ($a_m^{1.1°} = 16.9$ nm and $a_m^{0.9°} = 20.5$ nm). We note that comparing the wavefunction's size to the calculated moiré periodicity as an absolute number is a simplification, ignoring details about the shape of the wavefunction within the two-dimensional plane. For instance, some of the 2500 states for the smaller twist angles, e.g. 0.9°, exhibit rather one-dimensional quantum wire-like states along ridges of the potential landscape (cf. Fig. S6). Nonetheless, for most states and in general, the size given in Fig. 3d–f is a good indication of the wavefunction's (de)localization.

Calculation of optical spectra

Next, we discuss the calculated linear absorption spectrum of the computed states. In general, the temporal Fourier transform of the dipole-dipole correlation function $tr(\sigma_\alpha^-(t)\sigma_\alpha^+(0)\rho)$ (with $\sigma_\alpha^+ = |\alpha\rangle\langle g|$) yields the

Fig. 3 | Spatial extension of the excitonic states and absorption spectra for a varying twist angle. **a–c** Absolute value of the COM wavefunction of the first IX eigenstate in real space for a relative twist angle of (**a**) $\alpha = 1.3°$, (**b**) 1.1°, and (**c**) 0.9°. **d** In-plane size of the wavefunction with some adjustments for the periodic computation domain. We calculate the expectation value for all 2500 exciton eigenstates vs. their energy for 1.3° with each dot in the graph representing one state. The lowest-energy state, as in (**a**), is highlighted in red. The dashed horizontal line indicates the size of the moiré cell for the specific twist angle. **e, f** Corresponding representations for 1.1° and 0.9°. **g** Calculated linear absorption spectrum for the computed states at 1.3°. Gray area highlights the spectral range of the first states, as indicated by the gray area in (**b**). **h, i** Similar representations for 1.1° and 0.9°. Note that a zero detuning describes the lowest 1s IX energy without any influence from strain potentials. The shift to lower energies is consistent with a trend to exciton localization for smaller relative twist angles.
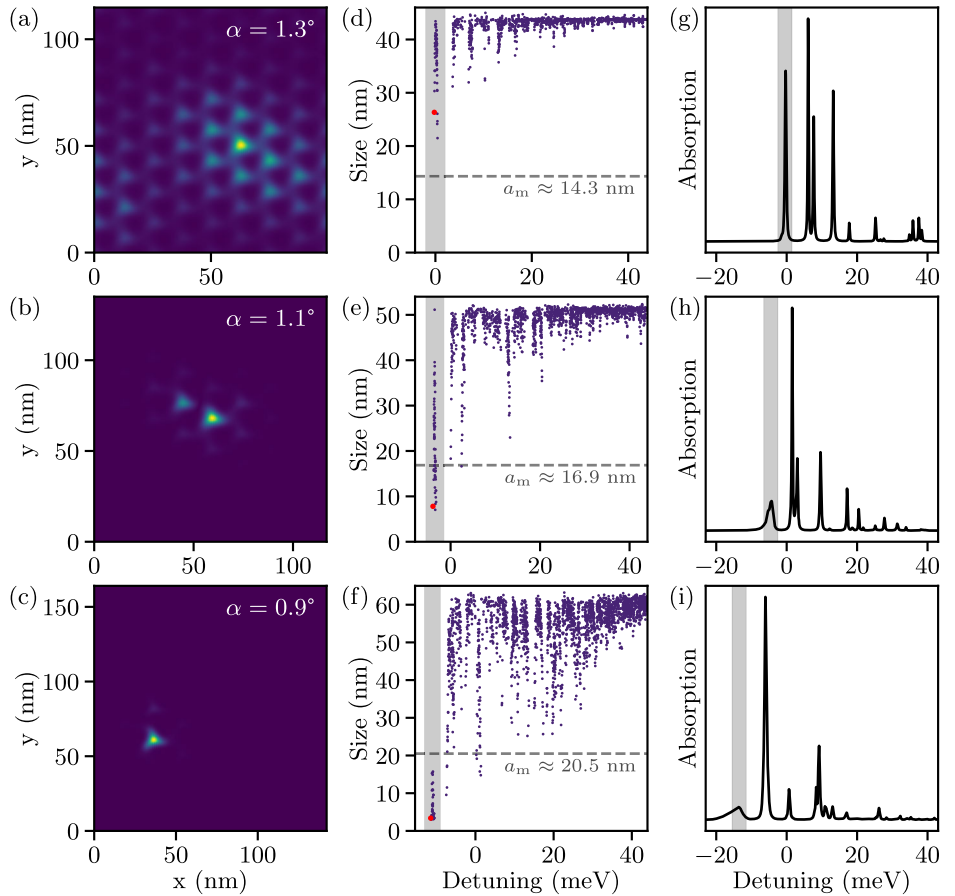
absorption lineshape $L_\alpha(\omega - E_\alpha)$ for an exciton state α centered around the exciton to ground state energy E_α. After applying the polaron transformation from the framework of ref. 32, the lineshape function becomes $\mathrm{tr}(\sigma_\alpha^-(t)B_-^\alpha(t)B_+^\alpha(0)\sigma_\alpha^+(0)\rho)$, where the operators $B_\pm^\alpha$ describe the nuclear reorganization initiated after exciton-photon interaction. A linear absorption spectrum $\alpha_{pp'}(\omega)$ for the incoming and detected polarization p and p' can be calculated via

$$\alpha_{pp'}(\omega) = \sum_\alpha \mathbf{D}_{\alpha g} \cdot \mathbf{e}_p \mathbf{D}_{\alpha g}^* \cdot \mathbf{e}_{p'}^* L_\alpha(\omega - E_\alpha), \quad (1)$$

with the coupling element $\mathbf{D}_{\alpha g} = \int d\mathbf{r} \mathbf{D}(\mathbf{r})\psi_\alpha(\mathbf{r})$, where $\mathbf{D}(\mathbf{r})$ uses a modification of definition from ref. 37 to include displacement due to strain (cf.[32] for details). Initially, before the excitation, there are no excitons present in linear absorption, and all bright exciton states can be accessed in the experiment. Figure 3g–i shows the linear absorption spectra for 1.3°, 1.1°, and 0.9° vs. the detuning energy, while a zero energy defines the lowest interlayer 1s exciton energy without the influence of the strain potentials. Note that all spectra in the following are averaged over calculations for slightly different strain fields made from the distribution of strain fields with different residual disorder. Furthermore, we include only one type of exciton: i.e. interlayer 1s excitons, in particular, so that signatures of singlet/triplet excitons[46] are not included in the simulation.

The gray areas in Fig. 3g–i highlight the exciton states with the lowest energy for each twist angle with a finite absorption strength within the disordered ensemble. Comparing Fig. 3g–i, it becomes obvious that the potential wells exhibit deeper minima for smaller twist angles. Moreover, our calculations imply an increasing spectral distinction between peaks with increasing twist angles. This is visible in the linear absorption spectrum and the energetic position of all 2500 states in the size plots. The increasing distinction is especially visible in the shape of the lowest peak, which

transforms from the asymmetric shape at 0.9° to the pure Lorentzian form at 1.3°. The trend reflects the transition from a distribution of clearly localized states with an Urbach tail visible in the spectrum at (0.9°)[47,48], to a mixture of delocalized and localized states (1.1°), and finally to only delocalized states (1.3° and above).

It is important to note that not all states within the linear absorption spectra are expected to be visible in photoluminescence, which explains the striking difference between the absorption spectrum for 1.3° as depicted in Fig. 3g and the corresponding photoluminescence spectrum introduced in Fig. 1d. The reason for the difference is discussed in the following. The photoluminescence spectra are calculated via the correlation function $\mathrm{tr}(\sigma_\alpha^+(t)\sigma_\alpha^-(0)\rho)$ (or after polaron transformation $\mathrm{tr}(B_+^\alpha(0)\sigma_\alpha^+(0)B_-^\alpha(t)\sigma_\alpha^-(t)\rho)$), where α indices the exciton state, which yields the photoluminescence lineshape function $L_\alpha^*(E_\alpha - \omega)$. The lineshape function for photoluminescence (mainly caused by electron-phonon interaction) is mirrored at the exciton energy E_α compared to the lineshape function in linear absorption. Note that the center of the lineshape function does not coincide with its maximum but with the zero phonon transition due to an imbalance of phonon emission and absorption processes. While for linear absorption all optically active states contribute, the emission in photoluminescence is determined by the exciton density distribution $\rho_{\alpha\alpha}$, which approaches a quasi-equilibrium Boltzmann distribution for a long time. Overall, the PL spectrum takes the form:

$$\mathrm{PL}_p(\omega) = \sum_\alpha \mathbf{D}_{\alpha g} \cdot \mathbf{e}_p \mathbf{D}_{\alpha g}^* \cdot \mathbf{e}_p^* L_\alpha^*(E_\alpha - \omega)\rho_{\alpha\alpha}, \quad (2)$$

assuming that it is measured on time scales long enough for the coherence induced by the exciting laser to have already decayed, and that the approximate steady-state limit can be applied to describe the emission process.
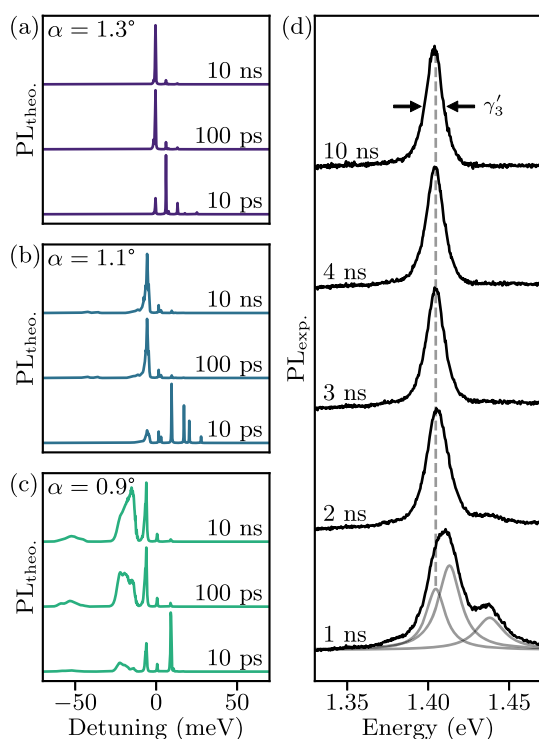
Fig. 4 | Time-resolved photoluminescence spectra of interlayer excitons.
a Calculated photoluminescence spectra for a heterostructure with a relative twist angle of 1.3° at time delays ranging from 10 ps to 10 ns with respect to the excitation pulse. The temperature is $T_{bath}^{theo} = 100$ mK. **b**, **c** Corresponding theoretical results for 1.1° and 0.9°. **d** Experimental time-resolved photoluminescence spectra of IXs at $T_{bath}^{exp} < 100$ mK. Excitation with a laser power of 150 nW and an energy of 1.937 eV. All spectra are normalized.

Time-resolved photoluminescence

Figure 4a shows calculated time-resolved photoluminescence spectra $T_{bath}^{theo} = 100$ mK for 1.3°. For the luminescence simulation, an initial Gaussian exciton density distribution of excitons at higher energies is assumed to mimic the scattering from intra-layer excitons. At short times in the 10 ps regime, the spectrum is dominated by emission lines at higher energies corresponding to a higher density population of IXs [cf. Figs. S7 and S8]. These lines have a direct correspondence to the ones in the linear absorption spectra [cf. Fig. 3g]. With the same argument, the amplitudes of the emission peaks vary as a function of time delay. Within a time-scale of tens to hundreds of ps, the energetically lowest state in PL increases in relative amplitude, i.e., the exciton states from the ground state peak dominate the photoluminescence at the longest times [cf. Fig. 4a]. This corresponds to the emission characteristic for an initially lower density of the IX population realized in experiment by a low excitation power and verified by a single Lorentzian-type emission line as in Fig. 1b (see also [cf. Figs. S7 and S8]). Figures 4b, c show equivalent theoretical photoluminescence spectra for 1.1° and 0.9° (cf. also Fig. S7). The overall dynamics is similar for the other angles, even though the nature of the involved states differs. Similar to the results for absorption, the main difference occurs in the lineshape variation and a varying spectral position of the levels.

In Fig. 4d, we complement the theoretical work with experimental time-resolved photoluminescence on sample 3 at $T_{bath}^{exp} < 100$ mK. Apart from the lowest energetic emission already discussed, the first spectrum at 1 ns delay features higher-lying excitonic states, which disappear for longer delays. We fit the spectrum by three Lorentzian curves with an FWHM of 14, 17, and 21 meV, respectively. Since the utilized CCD has a comparatively long gate time (2 ns), the first spectrum at a nominal time delay of 1 ns captures all events predicted by our calculations in the ps range. In turn, we

interpret the two higher-lying luminescence peaks to arise from an overlay of multiple excitonic states at an energy higher than the ground state, as depicted in Fig. 4a–c for short delay times. At later delay times of 2–10 ns, the lowest energetic emission dominates the photoluminescence and agrees qualitatively with the calculated spectra at 1.3°. The lines are much broader than in the measurement shown in Fig. 1b. The broadening is very likely caused by a larger area contributing to the signal in this particular experimental setup (as discussed below). Consequently, the experimental signal should be described by a weighted superposition of theoretical results of different twist angles, i.e. the results complement the interpretation of the experimental data originating from areas with a reconstructed heterostructure close to 1.3° on our samples, but likely with contributions reaching down to 0.9° and lower.

Discussion

Our calculations predict a comparatively flat potential for IXs at small twist angles relative to the 60° in H-type MoSe$_2$/WSe$_2$ heterostructures [e.g. Fig. 1c] and, consequently, the emergence of delocalized IX ground states with a spatial extension of several tens of nanometers (cf. Fig. 2). We note that predictions of the calculated spatial extension are merely limited by the computational domain and thus, computational power. Possible defects, sample edges, and cracks truncate the extension of the wavefunctions, but can still be considered in the simulations[32]. For a particular relative twist angle of 1.3°, we observe that a spatially extended ground state dominates the calculated luminescence for long times after excitation (>100 ps) [cf. Figs. 4a, 1d]. The corresponding absorption and luminescence exhibit a Lorentzian-type lineshape [cf. Figs. 3g, 1d] with a prevailing FWHM of γ_{theo} on the order of one meV [Fig. 1d], fundamentally limited by the electron-phonon interaction[32]. The spectral width and lineshape are sensitive measures of the IXs' interaction with their environment, and thereby, as demonstrated in Fig. 3, also for the localization and extension of the wavefunction in a spatially slightly varying potential landscape. As localization is related to the potential depths and disorder, it will particularly influence the luminescence energy and linewidth of localized states rather than the ones of delocalized states. In other words, the spatially integrated photon absorption and emission via localized IX states reflects the potential variation of the various moiré cells, where the IXs are generated or recombine [cf. Figs. 3h, i and 4b, c]. Note that the simulated potential variations based on the chosen disorder parameters due to incomplete reconstruction are on the order of 100s of μeV [e.g. arrow in Fig. 2a and Fig. S4] and that, in theory, a zero detuning describes the lowest 1s IX energy without any influence from strain potentials. In turn, Fig. 3g suggests that the Lorentzian-type lineshape evolves as soon as the impact of the potential variations is negligible, while localized states give rise to broadened non-Lorentzian lineshapes [Figs. 3h, i]. When all previous arguments are combined, it follows that, starting at 1.3° the underlying wavefunction of the lowest energy state is delocalized in the simulations, and a deviation from a Lorentzian-type emission may reflect the impact of the potential variations in the simulated area of a heterostructure.

Experimentally, we observe luminescence peaks on the investigated samples with a Lorentzian-type lineshape, which prevail down to excitation powers for which the signal is only limited by the apparent noise level of the utilized optical circuitry [Fig. 1b]. Comparing $\gamma_1 = 3.8$ meV of sample 1 to γ_{theo} [Fig. 1d], the experimental value reflects the imperfections of the investigated sample within the optical focus, but still, the observed Lorentzian-type lineshape suggests that the underlying wavefunctions are laterally extended (for γ_2, γ_3 of samples 2 and 3, see Fig. S1). Since we do not observe any blueshift of the emission energy of the experimental luminescence as in Fig. 1b, the investigated exciton ensembles can be considered to be in the dilute limit. In turn, the underlying IX states can be considered to be the lowest energy states that contribute to the luminescence in a quasi-stationary limit. Still, the time-resolved photoluminescence spectra at short time scales comprise light from states at higher energy. For instance, higher-lying states dominate the luminescence at short time scales [Fig. 4d and Fig. S8], which seems to be consistent with all of the shown, calculated spectra at

short time scales for α = 1.3°, 1.1°, and 0.9° [Fig. 4a–c], where exciton-phonon scattering eventually leads to relaxation towards the lowest IX state. On purpose, we present calculations for more than just one relative twist angle α to make clear that an experiment with an optical focus of one to two micrometers collects light from presumably many specific disorder-, strain- and moiré-potential variations, as well as corresponding IX states (cf. Figs. S7. For instance, the rather large value of γ'_3 = 11.5 meV for sample 3 as in Fig. 4d turns out to decrease to γ_3 = 7.5 meV when the heterostructure is measured in the setup as sample 1 in Fig. 1b (cf. Fig. S1) and the lineshapes become more Lorentzian. Furthermore, if we compare the experimental lineshapes at different positions of a sample (e.g. Figs. S9 and S10) to lineshapes of the calculated photoluminescence spectra for different angles (cf. Fig. 4a–c and Fig. S7 at 10 ns), we tentatively conclude that the lineshape can be a qualitative indicator for assigning the twist angles under investigation.

On a broader perspective, we note that the mentioned electron-phonon interaction is the fundamental limit of the observed experimental FWHMs as is consistent with previous measurements on the temporal coherence of IX ensembles with a Lorentzian-type luminescence profile[30,31]. The later publications report temporal coherence times of 100s of femtoseconds, which translates to an FWHM on the order of a few meV as is consistent with γ_{theo}. In other words, the measured Lorentzian-type lineshape can be understood to be dominated by a homogeneous broadening: namely, that for delocalized states, the physical interpretation allows for a momentum picture to account for the center-of-mass motion. In this picture, the emission results from low-energy, i.e., near-zero-momentum COM-states. Every scattering mechanism resulting in the occupation of non-zero COM momentum states is connected to dephasing. Last but not least, the deduced laterally extended wavefunctions of the IX ground states show the possibility of degenerate exciton ensembles in real samples of twisted TMD heterostructures with atomic reconstruction and small imperfections. We note, however, that the current work emphasizes a single-exciton delocalization, since it does not consider any exciton-exciton interactions as it would be needed to describe any transition to possible condensation and many-body phenomena of excitonic boson or fermion ensembles[49]. Exciton gas properties, including condensation effects, typically require a momentum-resolved description to discuss and compare their properties as closely as possible with respect to ideal, textbook-like quantum gases. Therefore, it is important to show that delocalized states can occur due to a dominating kinetic energy of the interlayer excitons in comparison to the moiré localization potential or the occurring disorder. We argue that delocalization at low densities is a prerequisite for observing exciton gas properties and many-body effects in analogy to ideal quantum gases. In order to experimentally disentangle the discussed single-exciton delocalization from possible many-body phenomena, a combination of experiments on the very same heterostructure seems to be necessary. This includes the demonstration of an extended spatial coherence of the luminescence[31], a reduction of the (Lorentzian-type) linewidth[30], and a (possible) increase of photon emission at zero momentum as detected in a back-focal plane geometry[50], all for an increasing number of excitons and a lowering of the bath temperature.

In conclusion, our work combines theoretical calculations of excitonic states in reconstructed MoSe$_2$/WSe$_2$ bilayers close to 60° with experimental photoluminescence measurements in equivalent samples. The calculations yield a potential for IXs within the strain-relaxed bilayers and random disorder, real-space excitonic wavefunctions, linear absorption spectra, and time-resolved photoluminescence spectra, as is consistent with earlier work[20,33]. Importantly, the theoretical results predict the reconstructed bilayer to exhibit a relatively flat potential landscape at 1.3° twist angle and above, with an energetically lowest state featuring a single Lorentzian-type photoluminescence peak. This peak also dominates for later times in the regime of quasi-equilibrium. Both predictions are consistent with our experiments, which include low-power as well as time- and spatio-resolved photoluminescence spectra at cryogenic temperatures. The calculated size of the wavefunction of the first COM IX eigenstates within the two-

dimensional plane at 1.3° twist angle suggests a delocalization of the exciton well beyond the moiré periodicity. Such a spatial extension is in agreement with the existence of degenerate interlayer exciton ensembles in similar MoSe$_2$/WSe$_2$ bilayers, but the current work does not consider any exciton-exciton interactions needed to describe any transition to possible condensation and many-body phenomena of excitonic boson or fermion ensembles[49], as well as lateral transport dynamics of IXs based on exciton-exciton and exciton-phonon interactions[51–54].

Methods

Experimental details
Our heterostructures are stacked with the PDMS method on SiO$_2$/Si substrates and encapsulated with hBN. We show photoluminescence data from three different samples 1, 2 and 3 (Fig. 1b, Fig. S1). All samples feature an H-type heterostructure close to 60° twist (Fig. S2). The widths of the lowest interlayer exciton emission peak are γ_1 = 3.8 meV, γ_2 = 3.3 meV and γ_3 = 7.5 meV. All power series show the lack of an energetic blueshift, suggesting negligible interparticle interactions within the investigated range of laser power. We note that the dilute limit mentioned in the main manuscript refers to this regime of negligible interactions between interlayer excitons. Moreover, spatial images of the excitonic photoluminescence are detected by utilizing a CCD camera, and the profiles are compared to the reflected laser profile (cf. Fig. S3). For the time-resolved photoluminescence spectra as in Fig. 4d of the main manuscript, we utilize a pulsed laser and a gated CCD. The detection CCD features a gate time of 2 ns. We use a pulsed laser diode (PicoQuant PDL 800-D) at 1.937 eV with a pulse duration of 70 ps. The repetition rate and the average power are set to 125 kHz and approximately 150 nW on the sample, respectively. The repetition frequency generates a time delay of 8 μs between the laser pulses that far exceeds the interlayer exciton lifetime.

Simulation details
The reconstructed strain maps are calculated by minimizing the strain field-dependent energy with a minimization algorithm using the numerical library TAO/PETSC[55], starting from a Gaussian random strain field distribution (though the dependence on the initial distribution is minimal). The minimization algorithm halts if a typical gradient accuracy for the energy minimization of Eq. (1) of ref. 32 of 0.1 meV/nm is reached or if the relative gradient is below 0.0001 (for details see TAO/PETSC documentation[56,57], for *TaoSetTolerances* and the parameters *gatol* and *grtol*). When varying this accuracy by one order of magnitude, we still observe stable luminescence spectra of the discussed excitons.

Data availability
The data analyzed in the current study are available from the authors (AWH for experimental data and MR for simulation results) upon reasonable request.

Code availability
The underlying code for this study is not publicly available for proprietary reasons.

References
1. Novoselov, K. S., Mishchenko, A., Carvalho, A. & Castro Neto, A. H. 2D materials and van der Waals heterostructures. *Science* **353**, aac9439 (2016).
2. Ajayan, P., Kim, P. & Banerjee, K. Two-dimensional van der Waals materials. *Phys. Today* **69**, 38–44 (2016).
3. Manzeli, S., Ovchinnikov, D., Pasquier, D., Yazyev, O. V. & Kis, A. 2D transition metal dichalcogenides. *Nat. Rev. Mater.* **2**, 1–15 (2017).
4. Wang, G. et al. Colloquium: excitons in atomically thin transition metal dichalcogenides. *Rev. Mod. Phys.* **90**, 021001 (2018).

5. Kormányos, A. et al. k.p theory for two-dimensional transition metal dichalcogenide semiconductors. *2D Mater.* **2**, 022001 (2015).

6. Xiao, D., Liu, G.-B., Feng, W., Xu, X. & Yao, W. Coupled spin and valley physics in monolayers of MoS$_2$ and other group-VI dichalcogenides. *Phys. Rev. Lett.* **108**, 196802 (2012).

7. Brotons-Gisbert, M., Gerardot, B. D., Holleitner, A. W. & Wurstbauer, U. Interlayer and Moiré excitons in atomically thin double layers: From individual quantum emitters to degenerate ensembles. *MRS Bull.* **49**, 914–931 (2024).

8. Rivera, P. et al. Observation of long-lived interlayer excitons in monolayer MoSe$_2$-WSe$_2$ heterostructures. *Nat. Commun.* **6**, 6242 (2015).

9. Miller, B. et al. Long-Lived Direct and Indirect Interlayer Excitons in van der Waals Heterostructures. *Nano Lett.* **17**, 5229–5237 (2017).

10. Hong, X. et al. Ultrafast charge transfer in atomically thin MoS$_2$/WS$_2$ heterostructures. *Nat. Nanotechnol.* **9**, 682–686 (2014).

11. Wilson, N. R. et al. Determination of band offsets, hybridization, and exciton binding in 2D semiconductor heterostructures. *Sci. Adv.* **3**, e1601832 (2017).

12. Nayak, P. K. et al. Probing evolution of twist-angle-dependent interlayer excitons in MoSe$_2$/WSe$_2$ van der Waals Heterostructures. *ACS Nano* **11**, 4041–4050 (2017).

13. Jauregui, L. A. et al. Electrical control of interlayer exciton dynamics in atomically thin heterostructures. *Science* **366**, 870–875 (2019).

14. Cao, Y. et al. Unconventional superconductivity in magic-angle graphene superlattices. *Nature* **556**, 43–50 (2018).

15. Jung, J., Raoux, A., Qiao, Z. & MacDonald, A. H. Ab initio theory of moiré superlattice bands in layered two-dimensional materials. *Phys. Rev. B* **89**, 205414 (2014).

16. Weston, A. et al. Atomic reconstruction in twisted bilayers of transition metal dichalcogenides. *Nat. Nanotechnol.* **15**, 592–597 (2020).

17. Rosenberger, M. R. et al. Twist angle-dependent atomic reconstruction and moiré patterns in transition metal dichalcogenide heterostructures. *ACS Nano.* **14**, 4550–4558 (2020).

18. Zhang, C. et al. Interlayer couplings, Moiré patterns, and 2D electronic superlattices in MoS$_2$/WSe$_2$ hetero-bilayers. *Sci. Adv.* **3**, e1601459 (2017).

19. Jin, C. et al. Observation of moiré excitons in WSe$_2$/WS$_2$ heterostructure superlattices. *Nature* **567**, 76–80 (2019).

20. Zhao, S. et al. Excitons in mesoscopically reconstructed moiré heterostructures. *Nat. Nanotechnol.* **18**, 572–579 (2023).

21. Fogler, M. M., Butov, L. V. & Novoselov, K. S. High-temperature superfluidity with indirect excitons in van der Waals heterostructures. *Nat. Commun.* **5**, 4555 (2014).

22. Alexeev, E. M. et al. Resonantly hybridized excitons in moiré superlattices in van der Waals heterostructures. *Nature* **567**, 81–86 (2019).

23. Steinhoff, A. et al. Exciton-exciton interactions in Van der Waals heterobilayers. *Phys. Rev. X* **14**, 031025 (2024).

24. Brotons-Gisbert, M. et al. Moiré-trapped interlayer trions in a charge-tunable WSe$_2$/MoSe$_2$ heterobilayer. *Phys. Rev. X* **11**, 031033 (2021).

25. Lagoin, C. & Dubin, F. Key role of the moiré potential for the quasicondensation of interlayer excitons in van der Waals heterostructures. *Phys. Rev. B* **103**, L041406 (2021).

26. Rossi, A. et al. Anomalous interlayer exciton diffusion in WS$_2$/WSe$_2$ Moiré Heterostructure. *ACS Nano.* **18**, 18202–18210 (2024).

27. Nielsen, C. E. M., da Cruz, M., Torche, A. & Bester, G. Accurate force-field methodology capturing atomic reconstructions in transition metal dichalcogenide moiré system. *Phys. Rev. B* **108**, 045402 (2023).

28. Seyler, K. L. et al. Signatures of moiré-trapped valley excitons in MoSe$_2$/WSe$_2$ heterobilayers. *Nature* **567**, 66–70 (2019).

29. Zhang, L. et al. Twist-angle dependence of moiré excitons in WS$_2$/MoSe$_2$ heterobilayers. *Nat. Commun.* **11**, 5888 (2020).

30. Sigl, L. et al. Signatures of a degenerate many-body state of interlayer excitons in a van der Waals heterostack. *Phys. Rev. Res.* **2**, 042044 (2020).

31. Troue, M. et al. Extended spatial coherence of interlayer excitons in MoSe$_2$/WSe$_2$ heterobilayers. *Phys. Rev. Lett.* **131**, 036902 (2023).

32. Richter, M. Theory of interlayer exciton dynamics in two-dimensional transition metal dichalcogenide heterolayers under the influence of strain reconstruction and disorder. *Phys. Rev. B* **109**, 125308 (2024).

33. Enaldiev, V., Zólyomi, V., Yelgel, C., Magorrian, S. & Fal'ko, V. Stacking domains and dislocation networks in marginally twisted bilayers of transition metal dichalcogenides. *Phys. Rev. Lett.* **124**, 206101 (2020).

34. Singh, R. et al. Localization dynamics of excitons in disordered semiconductor quantum wells. *Phys. Rev. B* **95**, 235307 (2017).

35. Richter, M., Singh, R., Siemens, M. & Cundiff, S. T. Deconvolution of optical multidimensional coherent spectra. *Sci. Adv.* **4**, eaar7697 (2018).

36. Khatibi, Z. et al. Impact of strain on the excitonic linewidth in transition metal dichalcogenides. *2D Mater.* **6**, 015015 (2018).

37. Wu, F., Lovorn, T. & MacDonald, A. H. Theory of optical absorption by interlayer excitons in transition metal dichalcogenide heterobilayers. *Phys. Rev. B* **97**, 035306 (2018).

38. Tran, K. et al. Evidence for moiré excitons in van der Waals heterostructures. *Nature* **567**, 71–75 (2019).

39. Ruiz-Tijerina, D. A., Soltero, I. & Mireles, F. Theory of moiré localized excitons in transition metal dichalcogenide heterobilayers. *Phys. Rev. B* **102**, 195403 (2020).

40. Fallahazad, B. et al. Shubnikov–de Haas oscillations of high-mobility holes in monolayer and bilayer WSe$_2$: Landau level degeneracy, effective mass, and negative compressibility. *Phys. Rev. Lett.* **116**, 086601 (2016).

41. Mostaani, E. et al. Diffusion quantum Monte Carlo study of excitonic complexes in two-dimensional transition-metal dichalcogenides. *Phys. Rev. B* **96**, 075431 (2017).

42. Jin, Z., Li, X., Mullen, J. T. & Kim, K. W. Intrinsic transport properties of electrons and holes in monolayer transition-metal dichalcogenides. *Phys. Rev. B* **90**, 045422 (2014).

43. Shree, S. et al. Observation of exciton-phonon coupling in MoSe$_2$ monolayers. *Phys. Rev. B* **98**, 035302 (2018).

44. Zimmermann, R., Runge, E. & Savona, V. in *Quantum Coherence Correlation and Decoherence in Semiconductor Nanostructures* Ch. 4 (ed. Takagahara, T.) 89–165 (Academic Press, San Diego, 2003).

45. Hermann, K. Periodic overlayers and moiré patterns: theoretical studies of geometric properties. *J. Phys.: Condens. Matter* **24**, 314210 (2012).

46. Fang, H. et al. Localization and interaction of interlayer excitons in MoSe$_2$/WSe$_2$ heterobilayers. *Nat. Commun.* **14**, 6910 (2023).

47. Urbach, F. The long-wavelength edge of photographic sensitivity and of the electronic absorption of solids. *Phys. Rev.* **92**, 1324–1324 (1953).

48. Piccardo, M. et al. Localization landscape theory of disorder in semiconductors. II. Urbach tails of disordered quantum well layers. *Phys. Rev. B* **95**, 144205 (2017).

49. Katzer, M. et al. Exciton-phonon scattering: competition between the bosonic and fermionic nature of bound electron-hole pairs. *Phys. Rev. B* **108**, L121102 (2023).

50. Sigl, L. et al. Optical dipole orientation of interlayer excitons in MoSe$_2$/WSe$_2$ heterostacks. *Phys. Rev. B* **105**, 035417 (2022).

51. Sun, Z. et al. Excitonic transport driven by repulsive dipolar interaction in a van der Waals heterostructure. *Nat. Photonics* **16**, 79–85 (2022).

52. Malic, E., Perea-Causin, R., Rosati, R., Erkensten, D. & Brem, S. Exciton transport in atomically thin semiconductors. *Nat. Commun.* **14**, 3430 (2023).

53. Wietek, E. et al. Nonlinear and negative effective diffusivity of interlayer excitons in Moir'e-Free heterobilayers. *Phys. Rev. Lett.* **132**, 016202 (2024).

54. Fowler-Gerace, L. H., Zhou, Z., Szwed, E. A., Choksy, D. J. & Butov, L. V. Transport and localization of indirect excitons in a van der Waals heterostructure. *Nat. Photonics* **18**, 823–828 (2024).
55. Balay, S., Gropp, W. D., McInnes, L. C. & Smith, B. F. in *Modern Software Tools in Scientific Computing* (eds Arge, E., Bruaset, A. M. & Langtangen, H. P.) 163–202 (Birkhäuser Press, 1997).
56. Balay, S. et al. PETSc Web page. https://petsc.org/ (2023).
57. Balay, S. et al. PETSc/TAO users manual. Tech. Rep. ANL-21/39 - Revision 3.19, Argonne National Laboratory (2023).

Author contributions
J.F., M.T., H.L., and T.S. performed the experiments. MR performed the theoretical calculations. A.W.H., U.W., M.R., and A.K. perceived the project. J.F., M.T., and J.K. fabricated the samples. T.T. and K.W. supplied the high-quality hBN. All authors contributed to the writing, read, and approved the manuscript.

Competing interests
The authors declare no competing interests.

Additional information
Supplementary information The online version contains supplementary material available at https://doi.org/10.1038/s41535-025-00820-0.

Correspondence and requests for materials should be addressed to Marten Richter, Andreas Knorr or Alexander W. Holleitner.

Reprints and permissions information is available at http://www.nature.com/reprints

Publisher's note Springer Nature remains neutral with regard to jurisdictional claims in published maps and institutional affiliations.